

Mechanical characterization of glass-ceramic scaffolds at multiple characteristic lengths through nanoindentation

Original

Mechanical characterization of glass-ceramic scaffolds at multiple characteristic lengths through nanoindentation / Shahgholi, Mohamad; Oliviero, Sara; Baino, Francesco; VITALE BROVARONE, Chiara; Gastaldi, Dario; Vena, Pasquale. - In: JOURNAL OF THE EUROPEAN CERAMIC SOCIETY. - ISSN 0955-2219. - ELETTRONICO. - 36:(2016), pp. 2403-2409. [10.1016/j.jeurceramsoc.2016.01.042]

Availability:

This version is available at: 11583/2642678 since: 2016-05-19T15:04:32Z

Publisher:

Elsevier

Published

DOI:10.1016/j.jeurceramsoc.2016.01.042

Terms of use:

This article is made available under terms and conditions as specified in the corresponding bibliographic description in the repository

Publisher copyright

(Article begins on next page)

Mechanical characterization of glass-ceramic scaffolds at multiple characteristic lengths through nanoindentation

Mohamad Shahgholi^a, Sara Oliviero^d, Francesco Baino^b, Chiara Vitale-Brovarone^b, Dario Gastaldi^a, Pasquale Vena^{a,c,*}

^a*Department of Chemistry, Materials and Chemical Engineering, Laboratory of Biological Structure Mechanics (LaBS) - Politecnico di Milano, Piazza Leonardo da Vinci 32, 20133, Milano, Italy*

^b*Institute of Materials Physics and Engineering, Department of Applied Science and Technology, Politecnico di Torino, 10129 Torino, Italy*

^c*I.R.C.C.S., Via R. Galeazzi 4, 20161, Milano, Italy*

^d*University of Sheffield, Department of Human Metabolism*

Abstract

The mechanical behaviour of implantable scaffolds is of relevant interest in all applications which require load-bearing capability. This study aims at establishing a quantitative relationship between the mechanical properties of glass-ceramic scaffolds for bone repair and the nano/micro-scale properties of their constituent materials. A nanoindentation study is carried out spanning different penetration depth on bulk (pore-free) glass-ceramic samples and on the walls of porous scaffolds. Micro-tomographical investigations allow assessing small-scale porosity of the scaffold walls. A simple homogenization model is used to establish the relationship between the elastic modulus of the bulk material and that of the micro-porous walls of the scaffolds. The elastic modulus of scaffold walls was found to be approximately 50% lower than that of the bulk glass-ceramic. The properties estimated experimentally on the walls of the scaffolds are quantitatively consistent with the analytical predictions provided by the homogenization model and the micro-porosity measured through tomographical analyses.

Keywords: Glass-ceramic, scaffold, Nanoindentation, micro-CT.

1. Introduction

The increase in average life expectancy is a great achievement of scientific findings; meanwhile, with aging population over the last decades, now bone re-

*Corresponding author

Email addresses: mohamad.shahgholi@gmail.com (Mohamad Shahgholi), sara.oliviero@libero.it (Sara Oliviero), francesco.baino@polito.it (Francesco Baino), chiara.vitale@polito.it (Chiara Vitale-Brovarone), dario.gastaldi@polimi.it (Dario Gastaldi), pasquale.vena@polimi.it (Pasquale Vena)

pair is one of the major clinical needs which requires significant research efforts
5 [1, 2]. Several studies have suggested the use of bioceramics, which include
biocompatible glasses, glass-ceramics and (crystalline) ceramics, for bone defect
healing and bone fracture treatment [3] in different regions of the body, i.e.
in vertebrae, maxillofacial reconstruction [4], hearing restorations (ear prosthe-
sis) [5], orthopedics, dental implants [6], [7], [8] etc. Bioactive ceramics **and**
10 **bioactive glasses** are able to create a stable interface with host tissue, and
some of them can even stimulate new tissue growth, which is crucial to pursue
clinical success in their applications [9]. In the early 1970s, Hench and cowork-
ers showed bioactivity of 45S5 bioglass [10]; from then various formulation of
bioglasses have attracted the interest **of the researchers in different tissue**
15 **repair applications** [11], [12], [13], [14], **and in the specific field of**
bone repair [15], [14],[16], [17], [18]. In this regard, the most important
role played by the scaffolds in bone tissue repair is the recovery of natural bone
functions [19], [20]. Specifically, major attention was devoted to optimizing the
design, composition and mechanical behaviour of porous bioactive glass-based
20 scaffolds for hard tissue recovery.

Often a three-dimensional (3-D) porous scaffold structure is fabricated by using
bioactive glasses in order to direct and support bone tissue growth and regener-
ation [21], [22]. Bioactive glasses are reported to stimulate more bone regener-
ation compared to other bioactive ceramics but they lag behind other bioactive
25 ceramics in terms of clinical success [15]. Hence, the number of research ac-
tivities on bioactive glasses is growing due to their unreached potential in the
market. In this work we deal with 3-D bioceramic sintered scaffolds fabricated
from the SiO_2 -based glass formulation CEL2 which was demonstrated to be
highly bioactive in vitro [23] and biocompatible with osteoblasts that expressed
30 the typical markers of osteogenesis [24], [25].The method selected for scaffold
fabrication, i.e. sponge replication, is able to produce highly-interconnected 3-
D network of open macropores [26] and trabecular structures characterized by
micro and nanopores. These peculiar features at different length scales substan-
tially affect the mechanical properties of the scaffold. **It is therefore of great**
35 **relevance to establish a characterization method that is able to de-**
termine the real mechanical properties of the glass-ceramic scaffold.
This method must explicitly account the features of the material
which are peculiar for the specific manufacturing approach: namely,
micro-porosity of the scaffold walls originated by the sintering pro-
40 **cess.** The specific aim of this study is to establish a quantitative relationship
between the mechanical properties of the glass-ceramic scaffold and the nano
and micro-scale properties of the constituent material with specific reference
to the material stiffness. This aim is achieved through an experimental and
analytical approach to the mechanical characterization of the scaffolds carried
45 out at multiple characteristic lengths. A nanoindentation study carried out at
multiple penetration depths (indentation loads) is integrated with analytical ho-
mogenization models and voxel-specific micro-CT data on 3-D porous scaffolds.
Very few papers are available on the application of nanoindentation
tests on ceramic scaffolds, among them Vivanco et al. [27] used

50 nanoindentation to characterize the mechanical properties of the scaffold walls with specific reference to the effect of the compliance of the micro-struts. More papers are available on micro-CT scan data used to assess the micro-porosity of the ceramic microstructures. Scheiner et al. [28] used micro-CT data to assess the microporosity of the
55 same glass-ceramic material investigated in this study. To the Authors' knowledge, the approach presented in this paper which puts together the micro-CT data and the nanoindentation data gathered at multiple characteristic lengths is novel. The mechanical characterization of the constituent glass-ceramic in a bulk form was the starting point of
60 this study. Unlike its bulk form, sintered glass-ceramic scaffolds exhibit small scale porosity which may heavily affect the mechanical properties of the scaffold wall. Thereby, the nanoindentation study carried out on the microstructure of the sintered scaffold will determine in a quantitative fashion the effect of the sintering process on the mechanical properties of the scaffold structural features.
65 Well-established analytical homogenization models are used to correlate the mechanical properties of the sintered structures with their nano- and microporosity. The porous structure as estimated through the analytical approach will be validated by making use of the attenuation data of micro-CT scans carried out on the glass-ceramic scaffolds.

70 2. Materials and Methods

2.1. Preparation of CEL2 bulk samples and scaffolds

An experimental SiO_2 -based glass formulation (CEL2; molar composition: 45% SiO_2 , 3% P_2O_5 , 26% CaO , 15% Na_2O , 7% MgO and 4% K_2O) was selected to produce the samples investigated in the present work. The glass
75 was prepared by melting the required quantities of high-purity reagents (powders of SiO_2 , $Ca_3(PO_4)_2$, $CaCO_3$, Na_2CO_3 , $(MgCO_3)_4Mg(OH)_2 \cdot 5H_2O$ and K_2CO_3 purchased from Sigma-Aldrich and used as received) in a platinum crucible in air ($1500^\circ C$ for 0.5 h to ensure homogeneity of the melt; heating rate $10^\circ C/min$). The melt was poured in stainless steel moulds (about
80 $50\text{ mm} \times 10\text{ mm} \times 10\text{ mm}$) and an annealing treatment ($500^\circ C$ for 12 h) was applied for glass thermal stress relaxation. The obtained glass bars were cut into 2-mm thick slices by using a diamond wheel (Accutom 5, Struers); these slices will hereafter be referred to as bulk samples. **The porous samples were obtained by means of the procedure described below.** The melt
85 was quenched into cold water to obtain a frit that was ground by ball milling (a six-ball zirconia milling machine was used), and the glass powders were eventually sieved through stainless steel sieves (Giuliani Technologies, Italy) to obtain a powder with a particle size below $32\ \mu m$. The 3-D scaffolds were produced by the sponge replication method, which was shown to be very effective to obtain
90 porous ceramics with a highly-interconnected 3-D network of open macropores [26]. Small cubic blocks ($10\text{ mm} \times 10\text{ mm} \times 10\text{ mm}$) of a commercial open-cell polyurethane (PU) sponge (45 ppi; density of the porous PU $\approx 20\text{ kg}/m^3$) were

coated with CEL2 powder by impregnation into a water-based glass slurry (glass : distilled water : poly(vinyl alcohol) (PVA) = 30 : 64 : 6 wt.%). After PVA
95 hydrolysis under continuous magnetic stirring at 80°C, CEL2 powder was added to the solution; the water evaporated during PVA dissolution was re-added to the slurry to restore the correct weight ratios among the slurry components. After further stirring for 15 min at room temperature to ensure slurry homogeneity, the sponge blocks were immersed in the slurry. The slurry infiltrated
100 the porous network of the PU template, that after 1 min was extracted from the batch and subsequently compressed ($\approx 50 \text{ kPa}$ for 1 s) up to 60% in thickness along three orthogonal spatial directions, in order to homogeneously remove the excess slurry; this infiltration/compression cycle was repeated for three times and a final cycle of impregnation alone was performed. The glass-coated sponges
105 were dried at room temperature overnight and afterwards thermally treated at 950°C for 3 h (heating and cooling rates set at 5 and 10°Cmin⁻¹, respectively) in order to burn-off the polymeric template and to sinter the inorganic particles. **A glass-derived replica of the starting PU template was finally obtained.** As reported elsewhere [26], two crystalline silicate phases develop
110 during the above-mentioned heat treatment; however, for the sake of simplicity, the expressions CEL2 scaffold or CEL2 sample will be hereafter adopted, without further specifying the glass-ceramic nature of the sintered materials. Consistently, the bulk samples were heat-treated according to the same conditions used to produce the scaffolds in order to obtain a material with the same
115 crystalline phases.

2.2. Embedding and polishing

Bulk and CEL2 samples were embedded in epoxy resin (Epofix, Struers) in order to facilitate the polishing procedure. Subsequently, a metallographic polishing wheel (Buehler) was used to perform 7 consecutive steps of polishing: 4
120 steps were performed using SiC sandpapers (grit sizes 600, 1200, 2500 and 4000) and 3 steps using adhesive papers (Alulap and Polilap) with alumina (Al_2O_3) suspensions (particle sizes 1 μm , 0.05 μm and 20 nm). Each step was performed at 100 rpm speed for 4 minutes in clockwise direction and 4 minutes in counter-clockwise direction. After polishing, samples were immersed in ultrasonication
125 bath (SONIC A) with deionized water for 7 times, 5 minutes each, in order to remove polishing debris. **A contact profilometry procedure was used to assess the average roughness over a $20\mu\text{m} \times 20\mu\text{m}$ square area of the polished surface. This was performed by using the Nanotest Platform described below and a tiny contact load (0.05 mN); an average roughness of approximately 100 nm was achieved.** The heterogeneous nature
130 of the sample surface did not allow us to obtain smoother surfaces. Due to this specific nature of the sample surface, indentation sites were selected manually on the basis of the microscopic imaging of the surface.

2.3. Nanoindentation tests

135 Three bulk samples and four porous samples underwent nanoindentation tests. Nanoindentation tests were performed on Nanotest Platform 3 (Micro-

Materials) at controlled temperature of $28^{\circ}C$ using a Berkovich diamond indenter. Load-controlled indentation tests were performed at 1, 50, 100 and 200 mN maximum load. For each load between 45 and 73 indentations were performed on the bulk samples, while between 11 and 33 tests were performed on the scaffolds. Loading and unloading rates were selected based on the maximum load, as shown in table 1. The peak load was held constant for a defined holding time depending on the maximum load (table 1). At the end of the test the load was held constant for 30 s at 10% of the maximum load; the measured displacement drift was used for the thermal drift compensation during post-processing. Diamond Area Functions (DAFs) and compliance values were calibrated on standard samples (fused silica) with standard procedures. Three different polynomial DAFs were used based on maximum penetration of the tip in the sample: a first DAF was calibrated for penetrations smaller than 200 nm, a second DAF for penetrations between 200 nm and 1400 nm, the ideal DAF was used for higher penetration depths. Analysis of the experimental curves was performed using the MicroMaterials software, which implements the Oliver-Pharr theory. Unloading curves were interpolated between 95% and 50% of maximum load for slope calculation. Nanoindentation modulus and hardness were obtained from each indentation curve. The nanoindentation modulus E^* is defined by:

$$\frac{1}{E^*} = \frac{1 - \nu_i^2}{E_i} + \frac{1 - \nu_s^2}{E_s} \quad (1)$$

Mechanical properties of the indenter (i) are known ($E_i = 1141 \text{ GPa}, \nu_i = 0.07$), therefore Young's modulus of the sample (s) can be calculated for a given Poisson's ratio (ν_s). The mechanical properties of the samples are identified by the reduced modulus M defined by:

$$\frac{1}{M} = \frac{1 - \nu_s^2}{E_s} \quad (2)$$

2.4. Morphological investigation

The morphology of scaffold at the macro- and micro-scale was investigated through Scanning Electron Microscopy at two different magnification levels: 100X and 2500X. The 100X images allowed us to identify the typical macro-pore size, while the 25000X images allowed us to assess the micro- or nano-porosity of the walls of the scaffold.

The inner porous network of CEL2 scaffolds was also non-destructively investigated by micro-computed tomography (Micro-CT; SkyScan 1174, Micro Photonics Inc.) to quantitatively assess the pore and strut features. Scanning parameters were selected as follows: source voltage 50 kV, current 800 μA , voxel size $13.73 \mu m \times 13.73 \mu m \times 13.73 \mu m$, exposure time per projection 8500 ms, rotation step 0.3° . The attenuation factors were converted in grey scale values and analysed to assess macro-porosity and nano-/micro-porosity of the material by means of a MATLAB code as described below.

Cubic Volume Of Interests (VOI) were identified in the whole analysed sample having different size and position within the sample. The edge size of the VOIs

ranged between $50 \mu m$ to $500 \mu m$. A built-in thresholding algorithm based on the Otsu's method was used to determine a global threshold with the purpose to identify pixels representing voids and pixels representing solid material (the latter being porous, i.e. micro/nano-pores had size smaller than the pixel size).
 180 Macro-porosity Φ^M is then obtained as follows:

$$\Phi^M = 1 - \frac{N_{solid}}{N_{tot}} \quad (3)$$

in which N_{solid} is the number of solid pixels and N_{tot} is the total number of pixels in the VOI.

The micro-porosity ϕ^μ is obtained by analysing the histograms of grey level distributions of all VOIs and by means of the following relationship:
 185

$$\phi^\mu = \frac{X - X_s}{X_{air} - X_s} \quad (4)$$

in which $X_s = 255$ is the grey level for the solid pixels at the peak of the histogram, while X_{air} is the grey level which corresponds to the peak of void pixels as obtained by identifying the peak in the histograms of each VOI.

2.5. Analytical model for porosity-mechanical properties relationship

190 A material is considered macro-homogeneous in continuum micromechanics if a micro-heterogeneous portion of it can form a representative volume element (RVE) [29]. The characteristic length l of a RVE should be such that $l \gg d$, where d is the characteristic length of the inhomogeneity within the RVE, and $l \ll L$, where L is the characteristic length of geometry/loading
 195 of the structure made by the material of the RVE. The microstructure within one RVE is not described in complete detail. In order to estimate the mechanical properties of the scaffold walls, the so-called Mori-Tanaka scheme [30] was applied, which has been previously used for similar scaffolds [28]. The Mori-Tanaka scheme was developed for composite materials with spherical inclusions
 200 and utilizes the bulk phases properties to estimate the homogenized modulus of the composite. For this application, a quasi-homogeneous portion of micro-porous material was selected within the scaffold walls as the RVE in order to apply the scheme. It was modelled as a composite where the solid phase is the bulk glass-ceramic material and inclusion material is air ($K_{air} = 0, G_{air} = 0$).
 205 Young's modulus for the dense material was obtained by nanoindentation on the bulk glass-ceramic samples, while Poisson's ratio was assumed 0.2766 [28]. By applying the Mori-Tanaka scheme, the homogenized bulk modulus $K_{sk}^{(hom)}$ and shear modulus $G_{sk}^{(hom)}$ can be estimated as a function of the scaffold wall micro-porosity ϕ^μ as:

$$K_{sk}^{(hom)} = \frac{(1 - \phi) K_{dg}}{(1 - \phi) + \frac{\phi}{1 - \alpha_{dg}}}; \quad G_{sk}^{(hom)} = \frac{(1 - \phi) G_{dg}}{(1 - \phi) + \frac{\phi}{1 - \beta_{dg}}} \quad (5)$$

210 where K_{dg} and G_{dg} are the bulk and shear moduli of the solid phase, while α_{dg} and β_{dg} are the volumetric and deviatoric part of the Eshelby tensor [31], respectively:

$$\alpha_{dg} = \frac{3K_{dg}}{3K_{dg} + 4G_{dg}}; \quad \beta_{dg} = \frac{6(K_{dg} + 2G_{dg})}{5(3K_{dg} + 4G_{dg})} \quad (6)$$

The homogenized Young's modulus is obtained by applying the classical relations of isotropic linear elasticity:

$$E_{sk}^{hom} = \frac{9K_{sk}^{hom}G_{sk}^{hom}}{3K_{sk}^{hom} + G_{sk}^{hom}} \quad (7)$$

215 The reduced modulus of the microporous material is therefore:

$$M_{sk}^{hom} = \frac{E_{sk}^{hom}}{1 - \nu_{sk}^{hom2}}; \quad \nu_{sk}^{hom} = \frac{3K_{sk}^{hom} - 2G_{sk}^{hom}}{6K_{sk}^{hom} + 2G_{sk}^{hom}} \quad (8)$$

In equations (5,6,7,8) the following relationships are used $K_{dg} = \frac{E_{dg}}{3(1-2\nu_{dg})}$, $G_{dg} = \frac{E_{dg}}{2(1+\nu_{dg})}$.

3. Results

3.1. Nanoindentation tests

220 Results from nanoindentation experiments on the bulk material are reported first. The nanoindentation moduli (E^*) and hardness are shown in figure 1. In all box plots the symbols represent the average measure at each load level, while the top and bottom bounds of the boxes represent the 95 percentile and 5 percentile of all experimental measures. Top and bottom whiskers represent
225 the extreme measured values. Outliers are reported with cross symbols.

The penetration depths ranged between 82 nm and 1300 nm, approximately; this indicates that the nanoindentation experiments spanned the characteristic lengths which covered one order of magnitude. No statistically significant difference was found between **measures at different loads for both indentation moduli and hardness**; this indicates that mechanical properties of the bulk
230 sample did not show dependence on the characteristic length of the experiments.

The average nanoindentation modulus was 105.98 GPa, which corresponds to a reduced modulus of 116.77 GPa and to an elastic modulus of 108.27 GPa, assuming a Poisson's ratio of 0.2766 [28]. This result was found to be consistent
235 with the one obtained using the impulse excitation technique (99.8 GPa).

Nanoindentation moduli and hardness obtained on the scaffold walls are reported in figure 2.

The penetration depth ranged between 43 nm and 1700 nm, approximately. A decreasing trend of the nanoindentation modulus with peak load was observed.
240 Significant differences were found between the distributions of nanoindentation

modulus obtained at different peak loads (Wilcoxon test, $p < 0.05$). No significant differences were found for hardness.

This size-dependence can be interpreted by inspection of the SEM images of the scaffold surface at high magnification (figure 3).

245 **As reported before, the image acquired at low magnification (figure 4) showed that the pore size of the macropores is larger than $100 \mu m$. Whereas, the image acquired at higher magnification showed that the scaffold walls are characterized by micro- and nano-porosity the typical size of which is smaller than $1 \mu m$.** In figure 3 the size of the
250 areas involved in indentations at different peak loads was schematically represented. It can be noticed that micro-porosity is not involved when applying 1 mN peak load, while indentations at higher loads involve a larger area affected by micro-porosity. The dependency of nanoindentation modulus on the applied load is then attributed to the porosity of the walls. In fact, the nanoindentation
255 modulus obtained at 1 mN peak load ($109.43 \pm 17.86 \text{ GPa}$) is comparable with those obtained on the bulk material, which does not exhibit porosity; while at 200 mN nanoindentation modulus decreased ($58.32 \pm 12.21 \text{ GPa}$) because the area involved in the test is porous.

260 3.2. Porosity and microstructure

As reported elsewhere [26], the development of two crystalline phases ($Na_4Ca_4(Si_6O_{18})$ and $Ca_2Mg(Si_2O_7)$) occurs upon sintering of CEL2 scaffolds, that are actually constituted by a glass-ceramic material.

The porosity of the starting PU template, assessed by micro-CT measurements, was 90 vol.%; the mean strut thickness and the mean pore size were about
265 $85 \mu m$ and $580 \mu m$, respectively. During the sponge replication process, the PU foam was coated with a thin and continuous layer of CEL2 particles in order to obtain, after the heat treatment, a glass-ceramic replica of the template. The total porosity of the scaffolds was estimated to range between 55 and 60 vol.%
270 by micro-CT analysis, that also revealed an excellent 3-D interconnectivity of the macropores (the open porosity was estimated to be above 95% of the overall porosity). The mean strut thickness and mean pore size were about $100 \mu m$ and $450 \mu m$, respectively. Macro-porosity was also observed by SEM (figure 4). In more details, figure 5 shows the values of macro-porosity as obtained from
275 eq. (3) for all considered sizes of the VOI. It is worth noting that for small VOIs a high dispersion of macro-porosity values was found at each VOI size. This means that macro-porosity is strongly dependent on the location of the VOI within the whole sample. Conversely, larger VOIs (larger than $400 \mu m$) showed less dispersed values of macro-porosity. This is an expected result as large portions of the VOIs overlap for size larger than $400 \mu m$. Figure 6 shows the value of micro-porosity as obtained from eq. (4) for all considered sizes of VOI. Also micro-porosity values exhibited high dispersion for small size VOIs; on the contrary, less dispersed values were obtained for VOI larger than $350 \mu m$. As discussed above, this is also an expected result. An average micro-porosity value
280 of 28% is found for the largest VOIs. Therefore elastic modulus and reduced

modulus of the glass-ceramic walls was obtained as a function of micro-porosity by applying equations 5,6,7. The normalized reduced modulus M/M_{dg} with $M_{dg} = 116.77 \text{ GPa}$ is shown in figure 7. **Both the reduced modulus obtained through the shallow indentations and that obtained through the deep indentations at 200 mN maximum load were used in the Mori Tanaka scheme to estimate the micro-porosity of the walls.** Reduced moduli obtained at 200 mN ranged from about 48.0 GPa to 75.0 GPa (average 61.4 GPa), which correspond to normalized reduced moduli ranging between 0.41 and 0.64 (average 0.54); therefore porosity was estimated to range from 0.21 to 0.38 (average 0.27). This micro-porosity range is consistent with that found through gray values of micro-CT scans; in particular, the average estimated micro-porosity (0.29) is consistent with the micro-porosity estimated through CT-scans **and the Mori Tanaka homogenization approach.**

4. Discussion

The aim of this paper was to assess the mechanical properties of glass-ceramic scaffolds allowing for micro- or nano-porosity at the microarchitectural level. The porous material was obtained by means of a sponge replica process. The characterization study was carried out by means of the nanoindentation tests performed at multiple characteristic lengths and analyses of micro-CT scans. Shallow penetration indentations on the walls of the porous structures showed elastic properties which were consistent with those found on the bulk glass-ceramic sample (i.e. without macro- and micro-porosity). Deep penetration indentations on the walls of the porous scaffold showed nanoindentation moduli which were lower than those found both at shallow penetrations on the scaffold and on bulk material. The shallow penetration depth was in the order of 50 nm which resulted in a contact diameter lower than the typical micro-porosity; on the contrary, the deep penetration depth was in the order of 1500 nm which is much larger than the typical nano- and micro-pores in the scaffold wall. This size comparison indicates that the mechanical properties determined at deep penetrations are affected by the porosity of the wall structure of the scaffold. This hypothesis has been confirmed by the estimation of the micro-nano-porosity of the walls obtained through the analyses of the micro-CT data. Indeed, a simple homogenization scheme for a micro- or nano-porous structure, the Mori Tanaka method, allowed us to estimate the porosity of the scaffold walls by comparing the reduced moduli found at shallow and deep indentations. The porosity of the walls assessed by micromechanical modelling (Eq.(5,6,7)) was consistent with that found through the micro-CT data analysis. Although it might be argued that the decrease of the indentation moduli with the penetration depth might be owed to damage or nano-fracture phenomena occurring locally under the indenter, the consistency between the micro-CT analysis and the nano-indentation results would actually exclude fracture phenomena. The surface roughness is, in general, a limiting factor for the reliability of indentation measures. In this study, average roughness was in the order of 100 nm (quadratic roughness estimate). This value was estimated over surface area

330 much larger ($20\ \mu\text{m} \times 20\ \mu\text{m}$) than the typical micro-pore size (about $1\ \mu\text{m}$),
which greatly affected the roughness measure. Indentation tests with loads
higher than 50 mN involved penetration depth higher than 500 nm; therefore
surface roughness was assumed to be suitable for indentations at these load lev-
els. Shallow indentations involved smaller contact area, therefore they were less
335 affected by the micro-pores.

**Pore size and trabecular thickness are comparable to those reported
by other authors for human healthy cancellous bone (radius and tibia)
[32]. This opens the route to new potential applications of these scaf-
folds as discussed in detail by Bairo et al. [33]. The mechanical
340 properties of the scaffold walls are higher than that exhibited by the
bone tissue at the trabecular level [34]; therefore further research is
needed. This study have shown that the micro-porosity of the scaffold
walls can be a morphological parameter which may be tuned with the
purpose to match the target mechanical properties.**

345 The assessment of the macroscopic stiffness and macroscopic strength of the
glass-ceramic porous scaffolds is also a relevant issue for a comprehensive me-
chanical characterization of such materials. This will be achieved in a future
study by means of CT-based finite element modelling in the linear and in the
non-linear range, along with the suitably designed macroscopic laboratory tests.

350

5. Conclusions

Bone-like glass-ceramic scaffolds with multiscale porosity have been pro-
duced by the sponge replication method. Mechanical properties of the scaffolds
at the scale of the single strut have been assessed in this work by means of a
355 nanoindentation study. The experiments have proven that the elastic modulus
of the scaffold walls is lower than that of the bulk material. Micro-porosity re-
sulting from SEM and micro-CT investigation on the porous scaffolds explains
the elastic mismatch with the bulk material which does not exhibit micro- or
nano-porosity. The approach reported in this work allows quantifying the effect
360 of the fabrication route (foam replica followed by sintering) on the mechanical
properties of scaffold struts.

6. Acknowledgements

The research leading to these results has received funding from the Italian
Ministry of University and Research (MIUR) in the frame of the PRIN project
365 Engineering physiologically and pathologically relevant organ Models for the
INvestigation of age related Diseases (MIND). The support provided by the
students Erica Rossi and Stefano Tagliabue on the analyses of micro-CT data
is kindly Acknowledged.

7. References

- 370 [1] J. Ebnezar, Textbook of Orthopaedics, JP Medical, 2010.
- [2] R. Cancedda, B. Dozin, P. Giannoni, R. Quarto, Tissue engineering and cell therapy of cartilage and bone, *Matrix Biology* 22 (1) (2003) 81 – 91. doi:[http://dx.doi.org/10.1016/S0945-053X\(03\)00012-X](http://dx.doi.org/10.1016/S0945-053X(03)00012-X).
URL <http://www.sciencedirect.com/science/article/pii/S0945053X0300012X>
- 375 [3] M. Vallet-Regi, E. Ruiz-Hernandez, Bioceramics: From bone regeneration to cancer nanomedicine, *Adv. Mater.* 23 (44) (2011) 5177–5218. doi:10.1002/adma.201101586.
- [4] L. Hench, M. Fenn, J. Jones, New materials and technologies for healthcare, World Scientific, 2011.
- 380 [5] K. R. Rust, G. T. Singleton, J. Wilson, P. J. Antonelli, Bioglass middle ear prosthesis: long-term results, *Am J Otol* 17 (3) (1996) 371–4.
- [6] S. V. Dorozhkin, Calcium orthophosphate-based bioceramics, *Materials* 6 (9) (2013) 3840–3942. doi:10.3390/ma6093840.
- 385 [7] L. Hench, J. Jones, F. MB (Eds.), New Materials and Technologies for Healthcare, World Scientific, 2011.
- [8] M. R. Norton, J. Wilson, Dental implants placed in extraction sites implanted with bioactive glass: human histology and clinical outcome, *Int J Oral Maxillofac Implants* 17 (2) (2002) 249–57.
- 390 [9] L. Hench, Bioceramics - from concept to clinic, *J. Am. Ceram. Soc.* 74 (7) (1991) 1487–1510.
- [10] L. Hench, The story of bioglass®, *Journal of Materials Science: Materials in Medicine* 0957-4530.
- [11] L. L. Hench, J. Wilson, Surface-active biomaterials, *Science* 226 (4675) (1984) 630–6.
- 395 [12] L. Hench, Bioceramics, *Journal of the American Ceramic Society* 81 (7) (1998) 1705–1728. doi:10.1111/j.1151-2916.1998.tb02540.x.
URL <http://dx.doi.org/10.1111/j.1151-2916.1998.tb02540.x>
- [13] M. N. Rahaman, R. F. Brown, B. S. Bal, D. E. Day, Bioactive glasses for nonbearing applications in total joint replacement, *Seminars in Arthroplasty* 17 (2006) 102 – 112, ceramic Bearings in Total Joint Arthroplasty. doi:<http://dx.doi.org/10.1053/j.sart.2006.09.003>.
URL <http://www.sciencedirect.com/science/article/pii/S1045452706000526>
- 400

- 405 [14] M. N. Rahaman, D. E. Day, B. S. Bal, Q. Fu, S. B. Jung,
L. F. Bonewald, A. P. Tomsia, Bioactive glass in tissue engineering, *Acta Biomaterialia* 7 (6) (2011) 2355 – 2373. doi:<http://dx.doi.org/10.1016/j.actbio.2011.03.016>.
URL <http://www.sciencedirect.com/science/article/pii/S1742706111001280>
- 410
- [15] J. Jones, Review of bioactive glass: from hench to hybrids, *Acta Biomaterialia* 9 (2013) 4457–86.
- [16] A. Hoppe, N. S. Guldal, A. R. Boccaccini, A review of the biological response to ionic dissolution products from bioactive glasses and glass-ceramics, *Biomaterials* 32 (11) (2011) 2757–74. doi:[10.1016/j.biomaterials.2011.01.004](https://doi.org/10.1016/j.biomaterials.2011.01.004).
- 415
- [17] A. A. Gorustovich, J. A. Roether, A. R. Boccaccini, Effect of bioactive glasses on angiogenesis: a review of in vitro and in vivo evidences, *Tissue Eng Part B Rev* 16 (2) (2010) 199–207. doi:[10.1089/ten.TEB.2009.0416](https://doi.org/10.1089/ten.TEB.2009.0416).
- [18] J. Chevalier, L. Gremillard, Ceramics for medical applications: A picture for the next 20 years, *J. Eur. Ceram. Soc.* 29 (7) (2009) 1245–1255. doi:[10.1016/j.jeurceramsoc.2008.08.025](https://doi.org/10.1016/j.jeurceramsoc.2008.08.025).
- 420
- [19] M. Braddock, P. Houston, C. Campbell, P. Ashcroft, Born again bone: tissue engineering for bone repair, *News Physiol Sci* 16 (2001) 208–13.
- [20] D. W. Hutmacher, Scaffolds in tissue engineering bone and cartilage, *Biomaterials* 21 (24) (2000) 2529–43.
- 425
- [21] L.-C. Gerhardt, A. R. Boccaccini, Bioactive glass and glass-ceramic scaffolds for bone tissue engineering, *Materials* 3 (7) (2010) 3867. doi:[10.3390/ma3073867](https://doi.org/10.3390/ma3073867).
URL <http://www.mdpi.com/1996-1944/3/7/3867>
- 430
- [22] F. Baino, C. Vitale-Brovarone, Three-dimensional glass-derived scaffolds for bone tissue engineering: current trends and forecasts for the future, *J Biomed Mater Res A* 97 (4) (2011) 514–35. doi:[10.1002/jbm.a.33072](https://doi.org/10.1002/jbm.a.33072).
- [23] C. Renghini, A. Giuliani, S. Mazzoni, F. Brun, E. Larsson, F. Baino, C. Vitale-Brovarone, Microstructural characterization and in vitro bioactivity of porous glass-ceramic scaffolds for bone regeneration by synchrotron radiation x-ray microtomography, *Journal of the European Ceramic Society* 33 (9) (2013) 1553 – 1565, cellular Ceramics. doi:<http://dx.doi.org/10.1016/j.jeurceramsoc.2012.10.016>.
URL <http://www.sciencedirect.com/science/article/pii/S0955221912006103>
- 440
- [24] C. Vitale-Brovarone, E. Verne, L. Robiglio, P. Appendino, F. Bassi, G. Martinasso, G. Muzio, R. Canuto, Development of glass-ceramic scaffolds

- for bone tissue engineering: characterisation, proliferation of human osteoblasts and nodule formation, *Acta Biomater* 3 (2) (2007) 199–208. doi:10.1016/j.actbio.2006.07.012.
- [25] G. Muzio, E. Vernè, R. A. Canuto, G. Martinasso, S. Saracino, F. Baino, M. Miola, L. Berta, R. Frairia, C. Vitale-Brovarone, Shock waves induce activity of human osteoblast-like cells in bioactive scaffolds, *J Trauma* 68 (6) (2010) 1439–44. doi:10.1097/TA.0b013e3181b28a8c.
- [26] C. Vitale-Brovarone, F. Baino, E. Verné, High strength bioactive glass-ceramic scaffolds for bone regeneration, *J Mater Sci Mater Med* 20 (2) (2009) 643–53. doi:10.1007/s10856-008-3605-0.
- [27] J. Vivanco, J. E. Jakes, J. Slane, H.-L. Ploeg, Accounting for structural compliance in nanoindentation measurements of bioceramic bone scaffolds, *Ceramics International* 40 (8, Part A) (2014) 12485 – 12492. doi:http://dx.doi.org/10.1016/j.ceramint.2014.04.103.
URL <http://www.sciencedirect.com/science/article/pii/S0272884214006543>
- [28] S. Scheiner, R. Sinibaldi, B. Pichler, V. Komlev, C. Renghini, C. Vitale-Brovarone, F. Rustichelli, C. Hellmich, Micromechanics of bone tissue-engineering scaffolds, based on resolution error-cleared computer tomography, *Biomaterials* 30 (12) (2009) 2411–9. doi:10.1016/j.biomaterials.2008.12.048.
- [29] A. Zaoui, Continuum micromechanics: Survey, *Journal of Engineering Mechanics* 128 (8) (2002) 808–816.
- [30] T. Mori, K. Tanaka, Average stress in matrix and average elastic energy of materials with misfitting inclusions, *Acta Metallurgica* 21 (5) (1973) 571–574.
- [31] J. D. Eshelby, The determination of the elastic field of an ellipsoidal inclusion, and related problems, *Proc R Soc Lond Ser A Math Phys Sci* 241 (1226) (1957) 376–396.
- [32] H. M. Macdonald, K. K. Nishiyama, J. Kang, D. A. Hanley, S. K. Boyd, Age-related patterns of trabecular and cortical bone loss differ between sexes and skeletal sites: a population-based hr-pqct study, *J Bone Miner Res* 26 (1) (2011) 50–62. doi:10.1002/jbmr.171.
- [33] F. Baino, S. Caddeo, C. Vitale-Brovarone, Using porous bioceramic scaffolds to model healthy and osteoporotic bone, *Journal of the European Ceramic Society* This issue.
- [34] E. Lucchinetti, D. Thomann, G. Danuser, Review: Micromechanical testing of bone trabeculae - potentials and limitations, *Journal of Material Sciences* 35 (2000) 6057 – 6064.

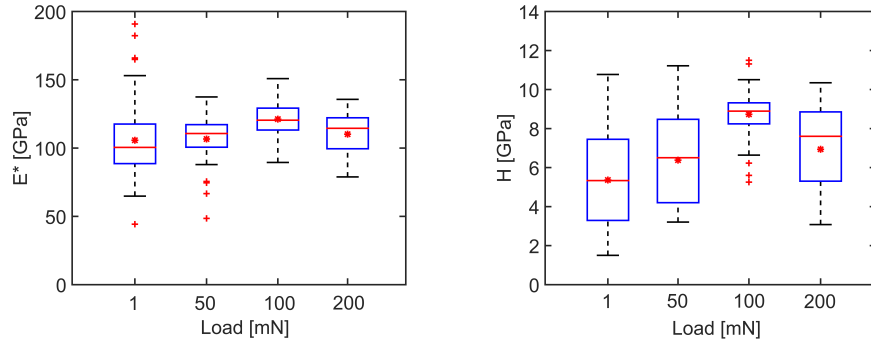


Figure 1: Nanoindentation modulus (left) and hardness (right) obtained from nanoindentation tests on the bulk material

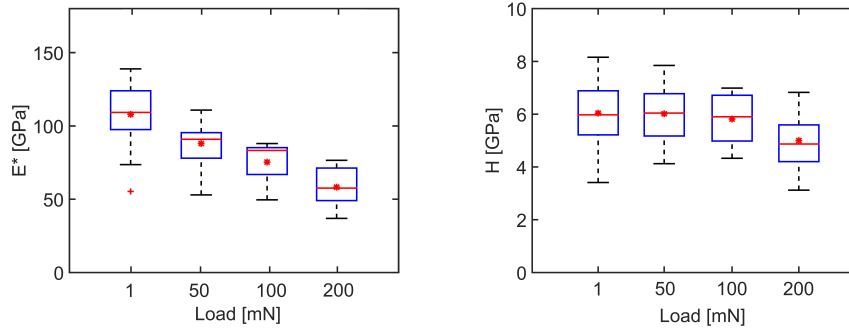


Figure 2: Nanoindentation modulus (left) and hardness (right) obtained from nanoindentation tests on the scaffold

Load [mN]	Loading rate (mN/s)	holding time [s]	unloading rate (mN/s)
1	0.5	30	0.5
50	2.5	3	5
100	2.5	3	5
200	2.5	30	5

Table 1: Parameters for nanoindentation tests

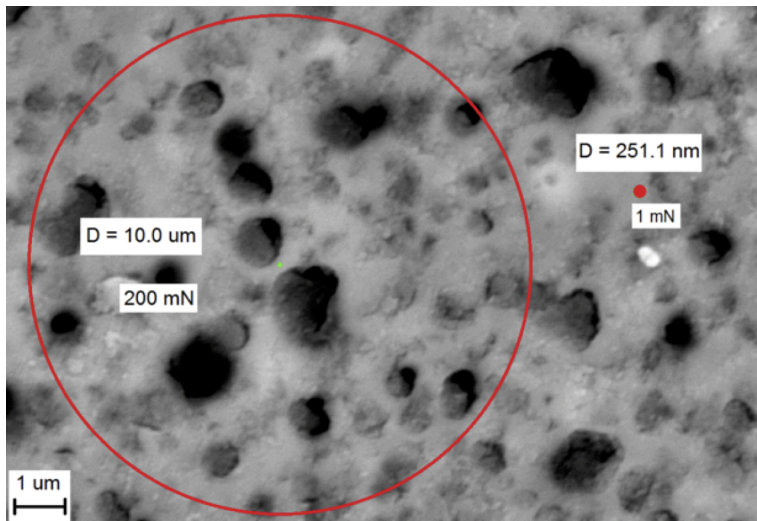


Figure 3: SEM image of the scaffold surface (magnification 25000x)

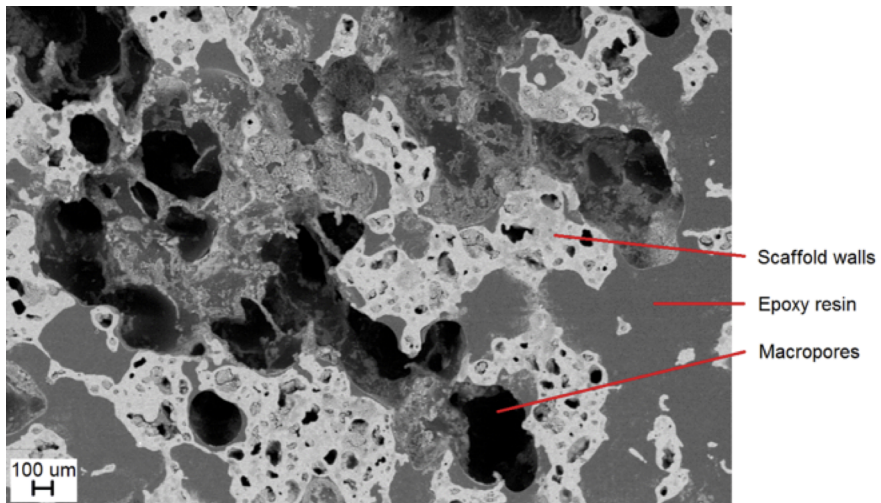


Figure 4: SEM image of the scaffold surface (magnification 100x)

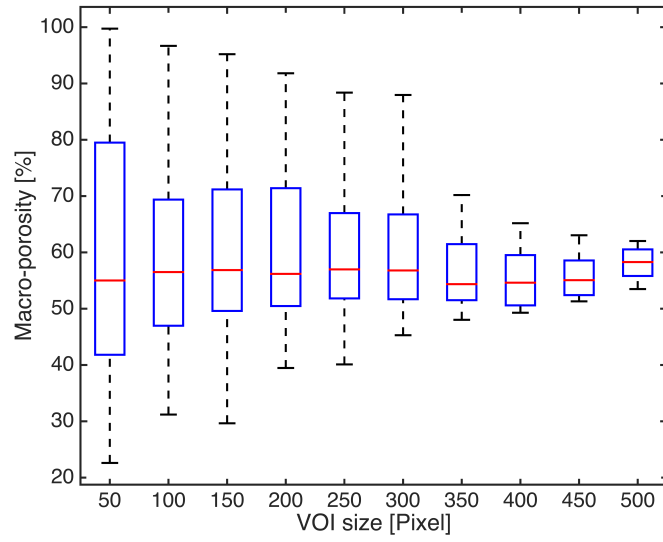


Figure 5: Macro-porosity estimated through the micro-CT data

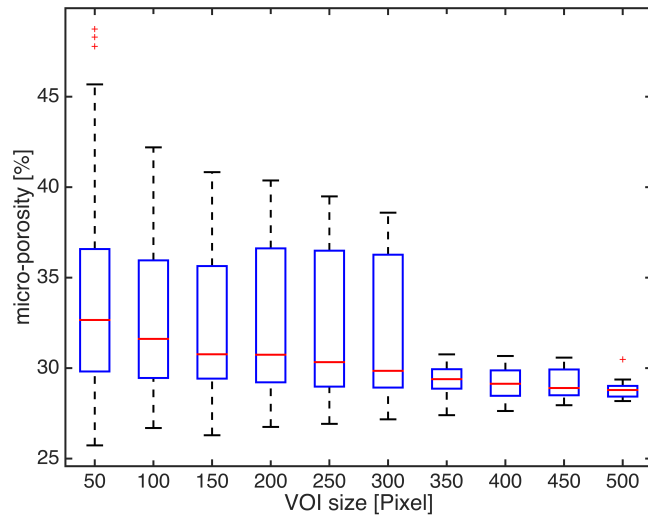


Figure 6: Micro-porosity estimated through the micro-CT data

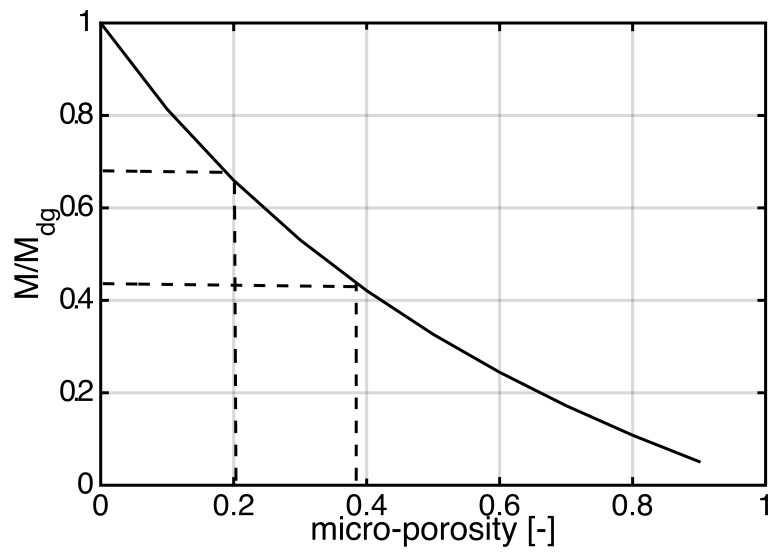


Figure 7: Mori-Tanaka estimate of the normalized reduced modulus vs micro-porosity